









Evaluation of MgZnCa Alloys Fabricated Via Powder Metallurgy for Manufacturing Biodegradable Surgical Implants

JORGE ALBERTO M. CARVALHO ^{1,2,7} GLÁUCIA DOMINGUES ^{3,8}
MÁRCIO T. FERNANDES ^{2,4,9} NILTON LARCHER ^{5,10}
ALEXANDRE A. RIBEIRO ^{6,11} and JOSÉ ADILSON CASTRO ^{2,12}

1.—Coordenação de Engenharia Mecânica, Centro Federal de Educação Tecnológica-Celso Suckow da Fonseca, Angra dos Reis, RJ, Brazil. 2.—Programa de Pós Graduação em Engenharia Metalúrgica, Universidade Federal Fluminense, Volta Redonda, RJ, Brazil. 3.—Coordenação de Engenharia Metalúrgica, Centro Federal de Educação Tecnológica-Celso Suckow da Fonseca, Angra dos Reis, RJ, Brazil. 4.—Departamento de Engenharia Mecânica, Faculdade Sul Fluminense, Volta Redonda, RJ, Brazil. 5.—Coordenação de Engenharia Mecânica, Instituto Federal do Espírito Santo, Aracruz, ES, Brazil. 6.—Divisão de Materiais-Instituto Nacional de Tecnologia, Rio de Janeiro, RJ, Brazil. 7.—e-mail: jorgeamc2014@gmail.com. 8.—e-mail: glaucia.domingues@cefet-rj.br. 9.—e-mail: teodoro_fernandes@id.uff.br. 10.—e-mail: tim.vi-larcher@gmail.com. 11.—e-mail: alexandre.antunes@int.gov.br. 12.—e-mail: joseadilson castro@id.uff.br

Biodegradable implants fabricated through powder metallurgy are not commonly observed but can be a good way to manufacture different alloys, reducing fabrication costs due to the net-shaped achievement. In this study, two different MgZnCa alloys, M1 (Mg₅Zn₁Ca) and M2 (Mg₂₉Zn₂Ca), processed by powder metallurgy, were investigated for their mechanical properties and corrosion resistance in a simulated blood fluid to check their viability as biodegradable devices. Complementary optical and scanning electron microscopy were also carried out to interpret the fabricated alloys microstructure characteristics. The M2 sample was found to be potentially usable as a biodegradable implant due to its results on mechanical resistance, hydrogenous dissolution, and corrosion reduction in comparison with the M1 sample, being adherent with other as-cast Mg alloys. Moreover, the degradation rate of the M2 alloy was found to be approximately 1mg cm⁻² day⁻¹ which is similar to other Mg-based alloys currently being used.

INTRODUCTION

Powder metallurgy (PM) can be used in different and combined ways to produce distinct engineering parts, being a good choice to achieve what is called “net-shape parts”, which usually reduce the final cost of the production of special devices. However, they are not commonly used to produce MgZnCa surgical implants.¹ In most cases, metallic implants manufactured by the metallurgical casting process are preferred. Their production procedure includes casting semifinished parts employing subsequent cold or hot subjection to improve the microstructure and mechanical properties, and, finally, net shaping through mechanical activity and finishing, to meet

the dimensional and surface quality requirements, which, in short, represent a large number of processes that will impact on the final implant cost. Despite their good biocompatibility, most metallic materials do not meet the biodegradation requirement.² Therefore, new materials with the capacity to improve the new standard of biodegradable surgical implants are in demand.^{2–4} In PM, the use of distinct powders to form different alloys in a variety of compositions can be a feasible opportunity to create more customized biodegradable implants, considering the particularities of human bone structure, thus enhancing the success of personalized treatments, and also reducing the implant cost.⁵ Moreover, new technologies in PM, such as metal injection molding combined with heat treatments,

(Received October 17, 2020; accepted May 24, 2021;
published online June 17, 2021)

are promising manufacturing methods when large quantities of complex-shaped surgical implants are required.⁵⁻⁷

According to the available literature, there is no consensus regarding the best alloy composition for the manufacture of Mg-based implants that meet biocompatibility and bio-absorption requirements.^{2,8} However, it is widely agreed that Mg alloys have properties that qualify them as biomaterials, such as high biocompatibility, very low toxicity, non-carcinogenic nature, low weight, compatible density, relatively low price, and ease of processing during manufacturing.³ Additional advantages of Mg over other metals are mechanical properties, such as low tensile modulus of elasticity, low density, good ductility, and mechanical strength. Furthermore, the concentration of Mg²⁺ in plasma is approximately 1.2–1.4 mM, its daily requirement in a human body is around 350 mg, and excessive Mg²⁺ can be excreted sufficiently in the urine.^{9,10} These properties are compatible with the structural and chemical properties of human bones, and justify the foundational use of this metal to produce suitable materials for surgical implant production.^{2,9}

Despite all these advantages, Mg has one major shortcoming: its high corrosion rate has limited its application in surgical implants. Among other candidate metals for bone structural implants, Mg presents the highest reactivity in the physiological environment conditions during bone recovery and consolidation. Its reactivity is approximately -2.34 V compared to the electric potential of hydrogen (NHE) at 25°C. In water, Mg exhibits a reactivity of approximately -1.75 V (NHE) due to the development of a protective film. This means that Mg will corrode faster than any other metallic material, especially in the presence of Cl⁻, HPO₄²⁻, HCO₃⁻, and SO₄²⁻ ions, which is the case in the human physiological environment and blood plasma.³ The reaction product of Mg in aqueous solutions is magnesium hydroxide (Mg(OH)₂). Mg dissolution is easily activated in a physiological environment due to the blood pH, which ranges from 7.0 to 7.4. At pH levels below 11.5, the solubility of Mg(OH)₂ increases, because the presence of chlorine ions in physiological liquids tends to result in the formation of highly soluble magnesium chloride (MgCl₂).⁴

The use of alloying elements such as Ca and Zn helps to mitigate the high propensity of Mg to corrosion. Ca in low proportions (<5%) can strengthen the alloy, either by solution or precipitation, and may refine grain size and contribute to the reinforcement of the grain boundary effects.⁴ Like Mg, Ca has a low density that is very close to that of human bone. Additionally, Ca is abundant in bone structure and essential for bone recovery.³ Zn can improve both the mechanical strength of Mg alloys and their corrosion resistance. It is also abundant in the human body, and therefore safe

for biomedical applications.¹¹ As an essential element, Zn is involved in bone metabolism and maintenance of its physiological function, and increases osteopathic phosphate activity in bone.^{12,13} Moreover, Zn and Ca are essential elements for humans, and they have relatively high daily allowance (~ 15 mg for Zn, ~ 0.8 g for Ca) and a large amount of storage. The release of Ca²⁺ from Mg alloys is beneficial to the healing and growth of bone,¹⁴ and Zn is known to influence bone remodeling.¹⁵ These properties make the use of Zn, Ca, and Mg to develop biocompatible and biodegradable surgical implants quite obvious; however, the amount of each element in the alloy is still debatable within the scientific community and calls for further investigation.

Diverse studies have presented different Mg alloy compositions. Most of them were obtained by casting in furnaces followed by additional mechanical and superficial treatment to improve and reinforce their mechanical and corrosion properties. Some, such as AZ31, AZ91, WE43, LAE442, MZX30, Mg-Ca, and Mg-Zn, among other alloys, have been explored; however, these have not been extensively used as surgical implants and none of them were produced by PM.^{15,16} Additionally, MgZnCa alloys have already been investigated as biodegradable materials in several reports.^{9,17-20} For example, the as-cast Mg₁Zn₅Ca alloy has been applied in clinical trials as bone-cast screws for hand and wrist fractures, showing complete replacement by the new bone within 1 year of implantation. The mechanical properties of this alloy, after annealing treatment, showed adequate mechanical strength, despite the low content of alloying elements (yield strength: 118 MPa, ultimate tensile strength: 198.8 MPa, and elongation: 12%).¹⁷

The use of PM as an alternative for the production of different alloy compositions may contribute to the attainment of implant devices with good potential in reducing the cost of industrial production, enabling customized treatments. These features can be considered innovative, and justify further studies on this subject with respect to searching viable and optimized implants with controlled properties and corrosion rates compatible with bone reconstruction and consolidation.

In this study, two different alloys of MgZnCa were produced using PM, Mg₅Zn₁Ca (M1) and Mg₂₉Zn₂Ca (M2), and their properties were evaluated to verify their applicability for surgical implants. The objective was to obtain Mg-based alloys with enhanced characteristics to be used as biodegradable biomaterials. The M1 sample was designed to have the alloying element content lowered to their solubility limit on the Mg matrix (6.2% and 1.35%, respectively, for Zn and Ca), and the M2 sample was designed to overcome these solubility limits by increasing the formation of the second phases and introducing grain refinement, as

these phenomena are recognized to reduce the internal galvanic corrosion in Mg alloys.¹⁸ The properties of the M1 and M2 alloys were evaluated with respect to their microstructure, corrosion resistance, and mechanical resistance, allowing comparison between them and with other as-cast alloys.

EXPERIMENTAL DETAILS

Alloy Fabrication

Powders of Mg, Zn, and Ca were supplied by the Military Chemical Laboratory (LQM) of the Brazilian Army of Technological Center (CTEx). The purity levels of the Mg, Zn, and Ca powders were obtained using a spectrometer of the fluorescence of x-rays (S8 Tiger/Software Spectra Plus 2.4.0.8; Bruker), and the results showed all the chemical elements identified in the form of percentages. The powders were then sieved in a vibrating machine model, T, and sieves from the Tyler series [circular shape, in stainless steel 2" high (c.5 cm)] (Pro-dutest). The sieving time adopted was 30 min for all the powders using the potentiometer of the vibrating machine in the eight position. Then, the material retained in each sieve was weighed. As a standard, the powders' dimensions were considered to correspond to the sieve where the powders were more retained. This procedure was repeated at least three times for each powder received, using 50 g each time (see supplementary text and Fig. S1).

First, the powders were weighed individually using a precision digital balance with a resolution of 0.001 g (AY220; Marte). Then, the powders were mixed for 30 min in a vibratory mill (MM-400; Retsch) at a frequency of 15 Hz. The compactations of the mixed powders were obtained by pressing them under a uniaxial load of 276 MPa using a die with a rounded surface of 74.5 mm² at room temperature ($\pm 25^\circ\text{C}$) and a total compact volume of approximately 1.3 cm³. These parameters were selected to obtain adequate green compact samples that could fit the sintering equipment under a controlled environment (see supplementary text and Fig. S2). After the compaction procedure, the samples were sintered in an argon environment at a heat rate of 10°C/min to 580°C and then maintained at a constant temperature for 60 min and cooled inside the furnace to room temperature ($\pm 25^\circ\text{C}$). A Netzsch-Dil 402C dilatometer was used to fabricate the alloys. From their sintering curves, it was possible to evaluate the sintering process by correlating their correspondent dilatation curves with the cohesions of the powders during the adopted rates of temperature and time. The chemical composition of the sintered alloys was analyzed by using X-ray fluorescence, showing a result of Mg (93.01 wt.%)-Zn (5.91 wt.%)-Ca (1.08 wt.%) for M1, and Mg (65.21 wt.%)-Zn (32.32 wt.%)-Ca (2.47 wt.%) for M2.

Alloys Characteristics and Corrosion Tests

After the sintering process, the samples were dry ground with SiC papers up to P2500, followed by polishing with 1- μm diamond paste, rinsing with distilled water, and drying with a warm air stream.

The microstructure evaluation was carried out by optical microscopy and scanning electron microscope (SEM) equipped with dispersive energy spectrum (EDS). An optical microscope (BX51M; Olympus), coupled with an Olympus SC30 digital camera, was used with the stream basic software (Olympus 8.1) to acquire images. For SEM analyses, an Inspect S50 (FEI), coupled with a tungsten filament (EVO-10; Zeiss), with a secondary electrons detector (JSM-5800; Jeol), was used. The microstructural characterization was performed at an open voltage of 20 kV.

The microhardness measurements were performed using a Dynamic Ultra-micro hardness tester (DUH211S; Shimadzu) fitted with a Vickers indenter. The test force used was 30 gf with a load speed of 1.0 gf/s, and a final holding time of 10 s before releasing the load. For each alloy, five specimens were assessed on the transverse section and the averaged values were recorded.

The corrosion behavior of the alloys was evaluated using the potential–dynamic polarization curve (PPC) and the degradation rate (DR) by hydrogen evolution on the environment. In these methods, the samples were tested in a simulated body fluid (SBF) called Kokubo solution.²¹ To account for the human physiological conditions, the pH of the SBF was adjusted to 7.4 and the temperature was maintained at 37 °C. These parameters were frequently monitored and kept constant during the corrosion tests.

The evaluations of specimens by PPC were carried out using the potentiostat/galvanostat equipment (Autolab PGSTAT204; Metrohm) and the data were collected by NOVA 2.1 software. For the three-electrode cell, a saturated calomel cell was used as a reference electrode, a platinum cell as a counter electrode, with a surface area of 1 cm², and the sample in the center as the working electrode. The electrochemical measurements were carried out at ± 300 mV using a 1-mV/s scanning rate. The tests were conducted in 100 mL Kokubo solution, being performed three times for the sake of replication. For the DR, the hydrogen evolution was monitored and converted to the sample DR using a mass balance. The hydrogen evolution measurements were taken as per the methodology described by Lu et al. Ref²². In brief, the funnel was placed upside down over the sample, and a measuring cylinder was positioned above the funnel. This configuration allowed for the collection of the hydrogen bubbles generated from the soaked sample, enabling the measurement of alloy degradation by calculating the height difference of the simulated body fluid used inside the measuring cylinder, using

a precision weight balance. The solution was maintained at 37 °C using an electrical thermo-controller. The increase in pH caused by the alloy's corrosion affects the DR, thereby requiring the solution to be refreshed every 24 h. The same protocol was used for all the measurements to compensate for this effect. After different immersion times, the soaked specimens were rinsed with ethyl alcohol and dried under cool air. Then, the alloy degradation was estimated based on the immersion time and hydrogen evolution.

RESULTS AND DISCUSSION

Powder Characterization and Sintering Evaluation

The results of the purity levels of the powders used in this study was obtained by X-ray fluorescence presenting 99.74%, 98.22%, and 99.57% for pure Zn, Mg, and Ca powders, respectively. Additionally, the X-ray fluorescence analyses found traces of other chemical elements with low content (see supplementary Table S1).

The dimensions of the powders were obtained through the sieving process. The dimensions of the Zn, Mg, and Ca powders were 0.025, 0.125, and 0.50 mm, respectively.

The dimensions, quantity, and morphology of the powders used to fabricate the alloys brought different behavior during the sintering process.

Both sintering curves for the M1 and M2 alloys are, respectively, depicted in Fig. 1a and b, showing the phase transformation temperature well discriminated by the dL/dt curve (dashed line). Phase transformation diagrams were used to interpret these curves, also inferred in Fig. 1c and d Ref ²³.

For the M1 sample (Fig. 1a), the first accommodation process occurs close to 230°C, when the alloy is going through the α -region (solid phase). Then, a high increment on the sample dilatation (dL) starts as the temperature reaches 480°C, keeping at the same rate up to 550°C, where the β -region shows up (eutectic phase). This behavior becomes softer as the sintering temperature goes through 570 °C and an internal accommodation seems to occur (dL/dt). During the period of 1 h at 580°C, the sample dimension keeps constantly dilating but at a lower rate.

The M2 sintering process presents a distinguishable behavior (Fig. 1b). The sample dilatation increases time by time as the temperature goes up at the heating rate of 10°C min⁻¹. After roughly 30 min of sintering, at about 300°C, when the alloy is going through the β -region, the first accommodation process is noticed. From this point on, up to about

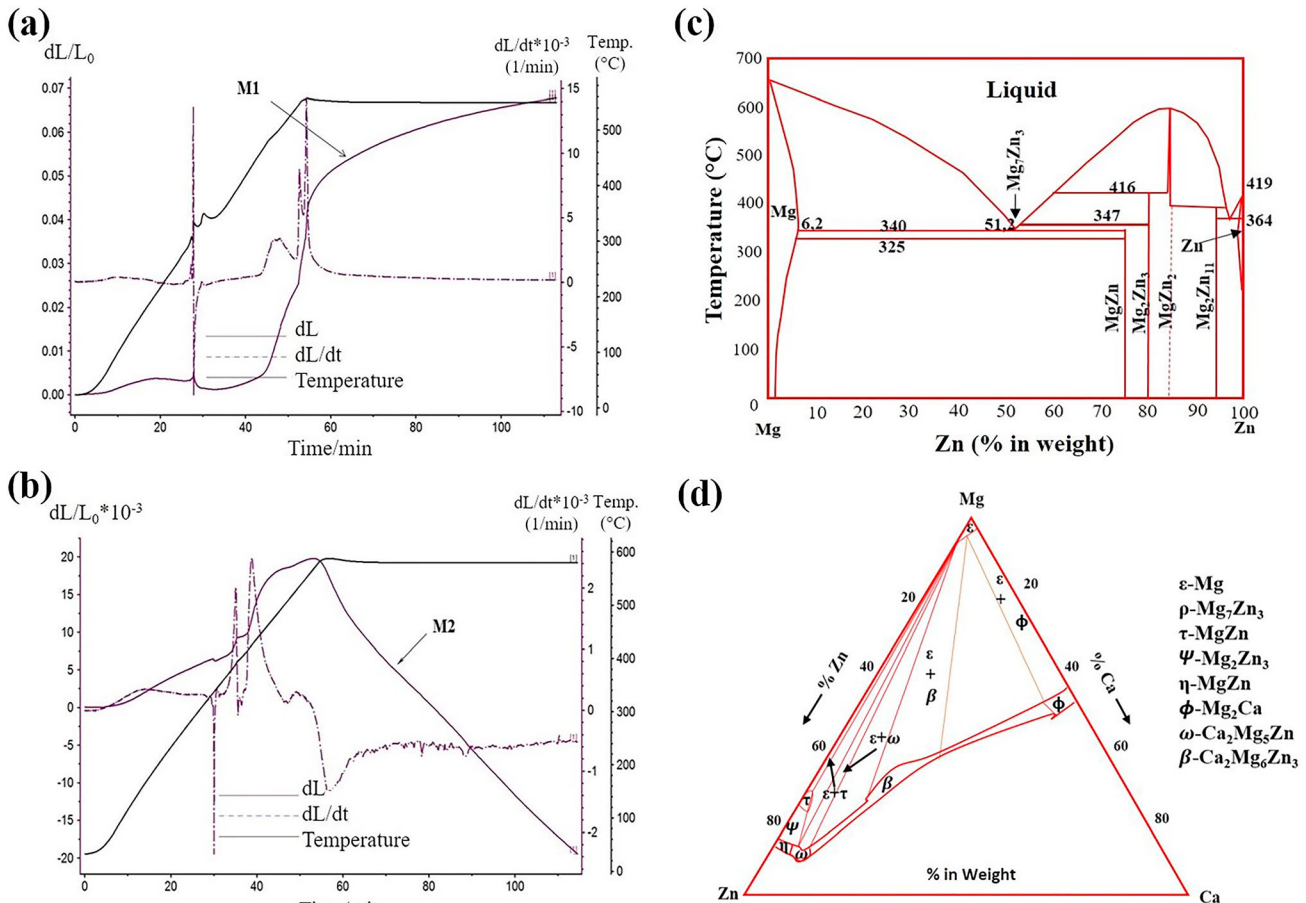


Fig. 1. Dilatometer curves for M1 (a), M2 (b), binary MgZn phase transformation (c), and ternary MgZnCa phase transformation (d).

380°C, when the alloy goes through the $\alpha + \beta$ region, a sample dilatation is enlarged. The sample seems to have an internal accommodation that has changed the dilatation curve gradient, but an increment in the sample dimensions is still noted (dL).

Furthermore, the sample suffers a soft dilatation process up to 580 °C. From this temperature on, a constant contraction occurs as the sample stays in the L-region (liquid phase). This sintering behavior is mostly related to the Zn and Ca content in the M2 sample, impacting the phase transformation temperature for this alloy.

Structure of the Fabricated Alloys

Five samples of each evaluated alloy with approximately the same dimensions in diameter and height (\varnothing 9.8 mm \times 17.5 mm) were fabricated, presenting a solid aspect, as Fig. 2 depicts.

The densities of the fabricated alloys were checked considering their final weight and dimensions. The densities were $1.486 \text{ g/cm}^3 \pm 0.008$ and $1.645 \text{ g/cm}^3 \pm 0.074$ on average, respectively, for M1 and M2. These values are potentially good, considering the effects of stress shielding between bone and implant, as they are similar to the natural human bone density ($1.8\text{--}2.1 \text{ g/cm}^3$ depending on the bone structure).²⁴ However, if just considering the individual powder elements densities (Mg– 1.74 g/cm^3 , Zn– 7.14 g/cm^3 , Ca– 1.53 g/cm^3) and their content in each fabricated alloy, we would expect a theoretical density close to 1.995 g/cm^3 for M1 and 3.292 g/cm^3 for M2. The differences between the theoretical densities and the calculated densities obtained can be related to the pore phase formed during the sintering process.

Pore Evaluation

In this study, the pore quantity was determined using the following expression²⁵:

$$\text{Pr} (\%) = (1 - p_R) \times 100 \quad (1)$$

where Pr (%) denotes the pore percentage and p_R denotes the relative density of the alloy, equivalent to the ratio between the calculated and theoretical densities (P_f/P_B) of the M1 and M2 alloys. Considering this verification, the Pr (%) was $25.52\% \pm 0.400\%$ and $50.02\% \pm 2.242$ for the M1 and M2 alloys, respectively.

Such a big difference between the porosity of the alloys was not investigated in detail and will be covered in further studies. However, a higher porosity was expected in M2 compared to M1 because of the greater presence of Zn and Ca in its composition. The suggestion put forth this is the higher barrier in the growth of internal grains in the M2 sample and its consequent refinement, which causes worse diffusivity of the elements involved in the alloy composition, generating porosity.²²

These results are important because, in the biomedical field, minimal porosity values are required for applications in cancellous, cortical, or trabecular bones.^{17,18} De Oliveira Ref²⁶ stated that higher interconnected porosity is crucial for the biocompatibility in macro-porous samples, usually associated with higher connectivity, offering suitable surgical implant applications. High degrees of porosity would lead to an interconnected porous structure, which would favor the cell ingrowth to porous space and vascularization and transport of metabolic products.^{17,25}

Microstructure and Morphology Characterization

The optical evaluation is presented in Fig. 3. The differences in the microstructure are related to the initial powder compositions, which, as already reported, have impacted the sintering process. In the two assessed alloys, M1 (Fig. 3a) and M2

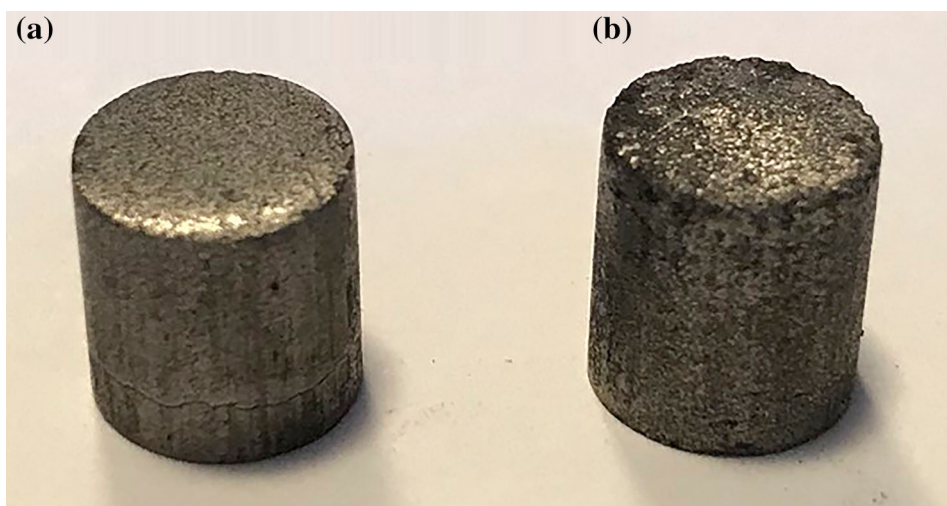


Fig. 2. Samples of fabricated M1 (a) and M2 (b) alloys.

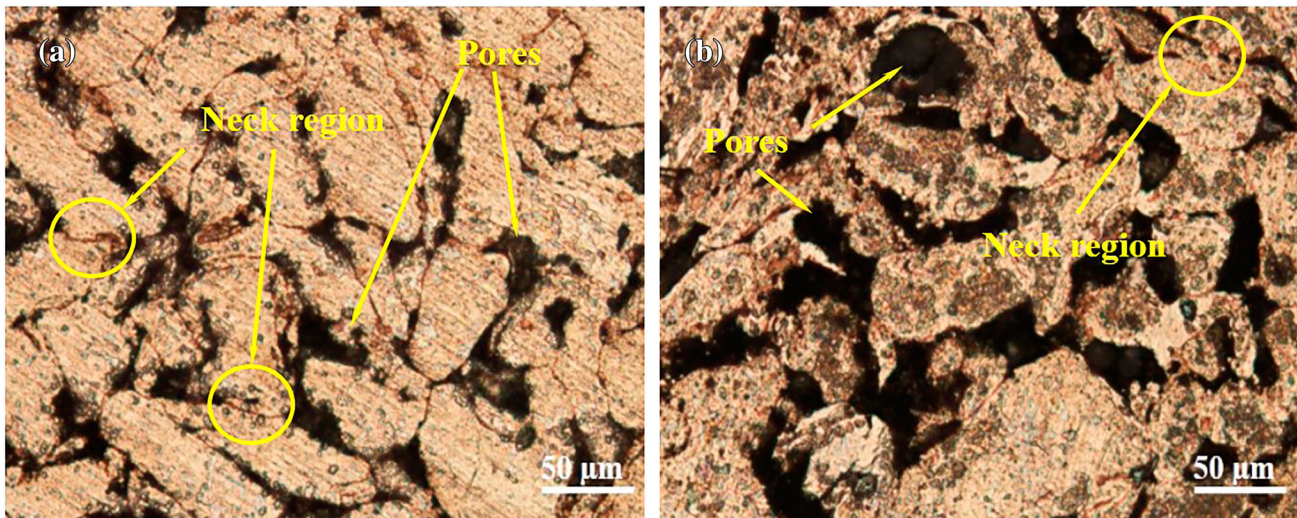


Fig. 3. Microstructures of the alloys (a) M1 and (b) M2; optical microscopy with no etching.

(Fig. 3b), we were able to identify the pores and neck regions with a good degree of cohesion, confirming the capacity of PM to fabricate structural alloys. The good distribution of the element components of the alloys can also be seen by EDS elemental mapping (see supplementary Fig. S3).

SEM images of M1 and M2 samples and EDS verifications are displayed in Fig. 4. The M1 sample (Fig. 4a) confirms that the α -Mg phase is dominant when the Mg content is dominant in the matrix (more than 93%).^{16,22}

For the M2 sample, Fig. 4b shows α -Mg phase with lamellar phases and some precipitation, confirming the results of previous studies that identified a relatively higher tendency of Mg alloys with high amounts of Zn and Ca to form a secondary phase.^{18,22} Moreover, some isolated α -Mg phases can be observed. Evidently, Zn has formed a solid solution in the Mg matrix and, when the content of Zn was higher than 5%, the microstructure has changed, allowing for the formation of a precipitate in the second phase and lamellar eutectic in the microstructure. The lamellar eutectic structures were mostly distributed in the grain boundary, and less distributed in the inter-dendrite areas, permitting the diffusion mechanism control and the grain refinement, as featured in red in Fig. 4a and b.

Additional verifications are depicted on Fig. 4c at four different points throughout the sample surfaces. The results confirm the combined effect of the varying amounts of Zn and Ca in the initial alloy, and the sintering parameters which can favor the formation of different phases and morphology, that in turn, determine both the mechanical and biocompatibility alloy properties. In Fig. 4c point 4, it can be seen that there are traces of sulfur (S) and silicon (Si) due to impurities of the individual powders. Their presence was already noticed by the X-ray fluorescence analyses (Sect. 3.1). It was expected that the secondary phases were mostly

Mg_4Zn_7 , Mg_7Zn_3 , and $\text{Mg}_2\text{Zn}_{11}$. However, the alloy's Ca content can contribute to the formation of MgZnCa phases with distinct compositions, such as $\text{Ca}_2\text{Mg}_6\text{Zn}_3$.^{18,19}

Based on the growth restriction factor (GRF) mechanism,^{22,24} the larger the values of GRF, the higher the refinement efficiency. The GRF is a measure of the segregating power of an element during solidification. The GRF values for Zn and Ca reach 5.31 and 11.94, respectively. Therefore, the Zn and Ca contents play important roles in controlling the growth of the nucleated grains and in further nucleation. Ca possesses a higher refinement efficiency and has a significantly high GRF, indicating its robustness at the solid-liquid interface of the new grains, thus preventing the extension of new grains into the melt. This is consistent with the studies conducted by Li et al. Ref²⁷ and Lu et al. Ref²², who reported that Ca segregation to the boundaries restricted grain growth, thus causing refinement. Zn and Ca strongly segregate in the melt and cause intense constitutional supercooling in the diffusion layer ahead of the advancement of the solid-liquid interface, promoting nucleation with grain growth restriction and, consequently, increasing the pore content in the alloy.^{24,25}

Surface Microhardness Evaluation

Alloy resistance was mechanically evaluated using a Vickers ultra-micro hardness tester at room temperature. For each alloy, five individual tests were carried out and the average values were considered for discussion. Table I summarizes the physical and mechanical properties obtained for M1 and M2 compared to natural bone and other Mg alloys collected from previous studies.^{10,17,22,28}

As shown, the elastic modulus obtained for the M1 and M2 samples are in the range of that of

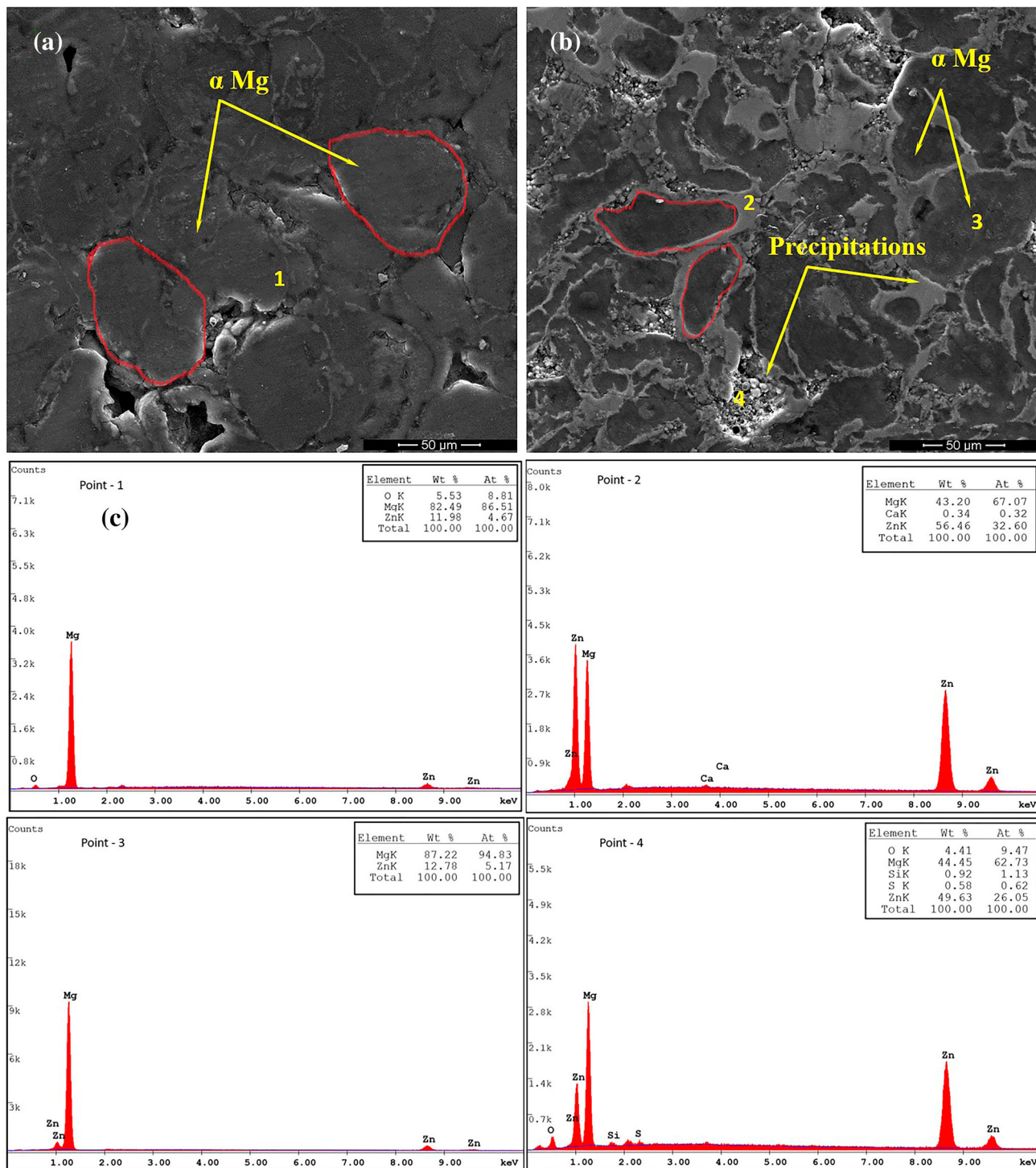


Fig. 4. SEM images of alloys (a) M1, (b) M2 and (c) EDS corresponding to points 1 to 4.

human bone but lower than the other Mg alloys. This aspect is very important for preventing the stress-shielding phenomenon during fractured bone reconstruction.²⁹

The superficial hardness for M1 and M2 samples are in the range of natural bone and other Mg alloys. M1 exhibited a lower Vickers hardness than

the others, suggesting a limited influence of the Zn and Ca contents in the Mg matrix. The M2 samples present a better result, very close to that of natural bone. It appears that the M2 sample had developed more precipitation phases and interstitial elements that positively impacted the superficial strength.

Table I. Physical and mechanical properties obtained for M1 and M2 in comparison to natural bone and other Mg alloys.

Property	Natural bone	Mg1Zn5Ca	AZ31	ZM20	M1	M2
Density (g cm ⁻³)	1.8–2.1	1.74–2.0	1.74–2.0	1.74–2.0	1.47–1.49	1.63–1.71
Elastic modulus (GPa)	3–20	–	–	32.1–32.7	13.0–15.0	17.0–23.0
Yield strength (MPa)	130–180	118–210	92.6–102.5	538.7–558.5	377.9–396.9	319.8–340.4
Hardness (HV)	26.2–42.1	–	60.0–70.2	49.8–51.6	33.8–36.8	38.8–44.6

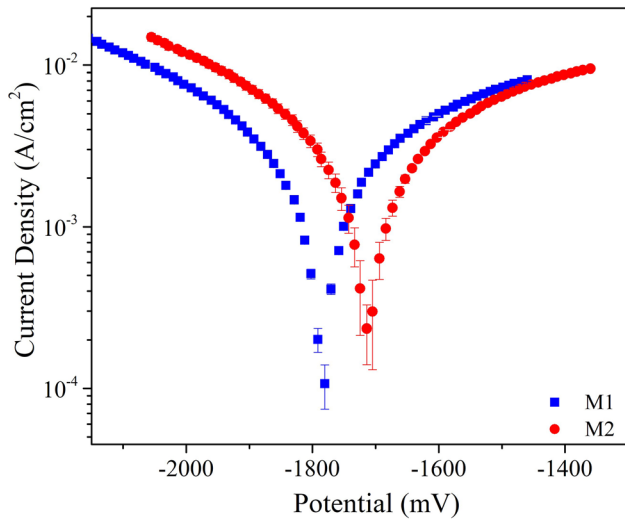


Fig. 5. Potentiodynamic curves for M1 and M2 samples in Kokubo solution at 37°C.

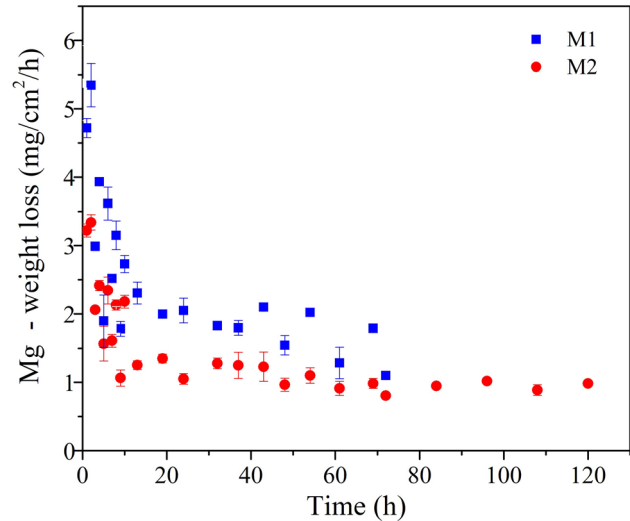
Potentiodynamic Polarization Evaluation

The potentiodynamic polarization curve for the two alloys is presented in Fig. 5. The corrosion potentials obtained for the alloys were -1781 mV for M1 and -1714 mV for M2, indicating that electrochemical reactions take place at the electrode–solution interfaces, and suggesting that the M2 sample exhibited a lower susceptibility to electrochemical reaction than the M1 sample. The corrosion potential values, j_{corr} , which are also inferred from the curves and is directly proportional to the corrosion rate for M1 and M2, were 1.29 mA/cm² and 1.05 mA/cm², respectively. Combining the higher E_{corr} and lower j_{corr} is expected to yield the best corrosion performance of the materials.^{29–32}

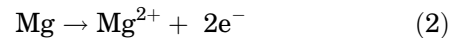
Degradation Rate (DR) Evaluations

The DR was assessed by monitoring the hydrogen evolution in the environment due to the formation of Mg(OH)₂. The monitored parameters were the Mg weight (in mg) of the corroded area and the exposure time of the specimen to the simulated physiological environment.^{22,33}

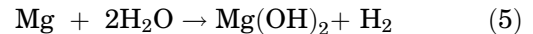
The mechanism of these reactions is easy to understand, assuming the Mg corrosion chemistry

Fig. 6. Degradation rate (mg cm⁻² h⁻¹) for M1 and M2.

in an aqueous environment as described in Eqs. (2), (3), and (4):



The overall reaction can be represented by Eq. (5):



Equation (5) shows that one mole of hydrogen corresponds to one mole of dissolved Mg in the physiologic solution. Considering that the hydrogen solubilized by the physiological solution corresponds to the same amount in weight loss of the alloy during the exposition time, these values can be converted to mg cm⁻² h⁻¹ as depicted in Eq. (6):

$$1 \text{ mL of H}_2\text{release} = 1,083 \text{ mg of Mg degraded} \quad (6)$$

For each alloy evaluated, M1 and M2, three samples were tested under the same conditions. The DR (Fig. 6) was clearly higher over the first 10 h; thereafter, the degradation rate tended to stabilize at different levels for each alloy.

The M1 samples did not remain intact for the total period of 120 h in contact with SBF, being completely degraded in approximately 72 h. The M2 samples suffered a certain level of degradation but kept as themselves until the final test period, or 120 h. Similar behavior was obtained for all three samples evaluated for each alloy (see supplementary Fig. S4).

Even presenting a structure with more pores, based solely on the evidence in the degradation analysis, the M2 sample maintains its structural state for a relatively and significantly longer period. After 48 h of exposure to SBF, its DR stabilized at close to $1.0 \text{ mg cm}^{-2} \text{ day}^{-1}$, consistent with the findings from previous studies on Mg-based alloys with additional mechanical, thermal, and coated treatments.^{27,29}

The M2 sample exhibited better corrosion resistance, and the chemical effect was reduced, further preserving its metal base. This can be attributed to the microstructure of the alloy formed using more Ca and Zn content. Moreover, the galvanic and pitting corrosion in the M2 alloy seems to be alleviated by a possible stronger passivation film, which could maintain and control the alloy dissolution during the exposure period. This is a favorable property for biodegradation and application to self-absorption implants (see supplementary results and discussion, and Fig. S5). Previous studies have indicated that the Zn content presents such a behavior. There is a strong relationship with the Zn presence in MgZnCa alloys that elevate and strengthen the distribution of galvanic regions in the alloys, which decisively impact its corrosion rate.^{15,22,33–35}

Cumulative Weight Loss Equations

The cumulative mass loss for each evaluated alloy (mg cm^{-2}) as a function of the square root of time

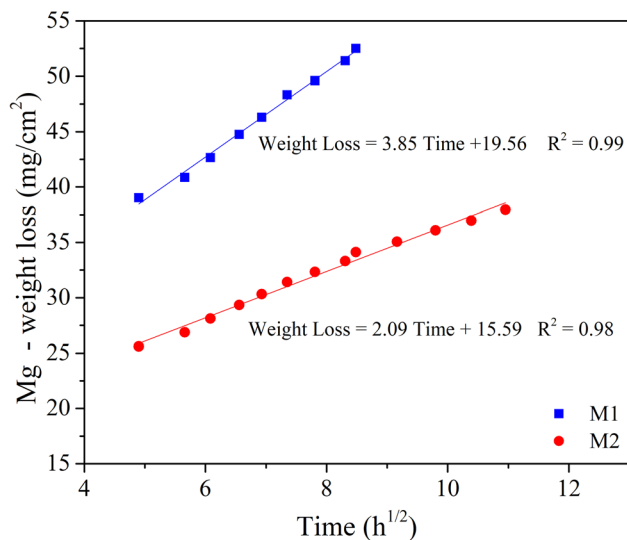


Fig. 7. Cumulative weight loss (mg cm^{-2}) for M1 and M2 samples over the exposition time ($h^{1/2}$).

($h^{1/2}$) is presented in Fig. 7. The time unit was suitable to ease the evaluation of the degradation behavior. The linearization of the curves has resulted in modeled equations as expressed by $(3.85 \times h^{1/2} + 19.56)$ and, $(2.09 \times h^{1/2} + 15.59)$, respectively, for M1 and M2. Following the presented equations, the cumulative degradation for M1 after 1 year of exposition is $\sim 2.55 \text{ mm y}^{-1}$, and 1.28 mm y^{-1} for M2. Following the results achieved, the M2 sample exhibited corrosion properties in compliance with the required structural function during the fractured bone trauma consolidation, which is usually at least 12 weeks.^{30,34}

The DR of M1 sample is not adherent with the currently degradable biomaterial and should be improved. Although presenting an intense initial DR, the M2 sample subsequently maintained an almost stable degradation of $1.0 \text{ mg cm}^{-2} \text{ day}^{-1}$. Compared to other alloys in use (see supplementary Table S2), the corrosion evaluation results have showed adherent values yielded by other as-cast alloys after being annealed, extruded, and coated with hydroxyapatite.^{10,17,22,28,30,31,34}

CONCLUSION

Powder metallurgy was used to produce MgZnCa alloys. The microstructure, degradation rate, and mechanical properties of the fabricated alloys were evaluated. Based on the achieved results, it has been shown that the powder metallurgy successfully produced near-shaped MgZnCa alloys, such as M1 (Mg5Zn1Ca) and M2 (Mg29Zn2Ca), with a presence of pores, in which, upon evaluation, the M2 sample exhibited stronger resistance and lower corrosion in SBF solution, yielding an average degradation rate of $1.0 \text{ mg cm}^{-2} \text{ day}^{-1}$, which is similar to other annealed, extruded, and hydroxyapatite-coated as-cast alloys.

It has also been shown that Zn and Ca content in the Mg alloys has a significant impact on their microstructure, and that one of the fabricated alloys (M2) exhibited more intermetallic and lamellar phases, as well as precipitate formation, mainly in the grain boundaries and dendritic regions, impacting in its grain refinement and pore formation.

Finally, the M2 sample yielded good results with regard to its microstructure balancing properties, corrosion resistance, and mechanical properties, and thus can be considered for use in surgical implants with suitable biodegradability characteristics. For further studies, evaluations of the adequate element composition of the powders, the sintering process parameters, and the consequence and cause of the pore formation in the MgZnCa alloy matrix should be explored for the development of customized surgical implants with self-absorption characteristics.

ACKNOWLEDGMENTS

We acknowledge the support of the Federal Center of Technology Education - Celso Suckow da Fonseca - Angra dos Reis in the development of this work. We are grateful to Fluminense Federal University - Metallurgical Engineer School - Volta Redonda; National Institute of Technology for the technical support; National System of Nanotechnology Laboratories (MCTI/SisNANO/INT-CEN-ANO-CNPq Process number 442604/2019-0) for financial support, and Military Chemical Laboratory (LQM) of the Army Technological Center (CTEx).

FUNDING

This paper did not receive any specific grant from funding agencies in the public, commercial, or non-profit sectors.

CONFLICT OF INTEREST

The authors declare that they have no conflict of interest.

SUPPLEMENTARY INFORMATION

The online version contains supplementary material available at <https://doi.org/10.1007/s11837-021-04739-2>.

REFERENCES

1. M. Bram, T. Ebel, M. Wolff, A.P. Cysne Barbosa, and N. Tuncer, *Advances in Powder Metallurgy*, 1st edn. (Woodhead, Sawston, 2013), pp 520–554.
2. F. Witte, *Acta Biomater.* 6, 1680. (2010).
3. P.-R. Cha, H.-S. Han, G.-F. Yang, Y.-C. Kim, K.-H. Hong, S.-C. Lee, J.-Y. Jung, J.-P. Ahn, Y.-Y. Kim, S.-Y. Cho, J.Y. Byun, K.-S. Lee, S.-J. Yang, and H.-K. Seok, *Sci. Rep.* 3, 2367. (2013).
4. J. Walker, S. Shadanbaz, T.B.F. Woodfield, M.P. Staiger, and G.J. Dias, *J. Biomed. Mater. Res. B* 102, 1316. (2014).
5. M. Wolff, J.G. Schaper, M. Dahms, T. Ebel, K.U. Kainer, and T. Klassen, *Powder Metall.* 57, 331. (2014).
6. J.G. Schaper, M. Wolff, B. Wiese, T. Ebel, and R. Willumeit-Römer, *J. Mater. Process. Technol.* 267, 241. (2019).
7. M. Wolff, J.G. Schaper, M.R. Suckert, M. Dahms, F. Feyerabend, T. Ebel, R. Willumeit-Römer, and T. Klassen, *Metals* 6, 118. (2016).
8. A. Dehghan-Manshadi, P. Yu, M. Dargusch, D. StJohn, and M. Qian, *Powder Technol.* 364, 189. (2020).
9. P. Ding, Y. Liu, X. He, D. Liu, and M. Chen, *Bioact. Mater.* 4, 236. (2019).
10. M.T. Fernandes, L.M. da Silva, B.X. de Freitas, G. Domingues, J.A. de Castro, and C. dos Santos, *Int. J. Mater. Res.* 111, 511. (2020).
11. X. Li, Y. Wang, C. Chu, L. Han, J. Bai, and F. Xue, *J. Mech. Behav. Biomed. Mater.* 105, 1751. (2020).
12. M. Nagata, and B. Lönnerdal, *J. Nutr. Biochem.* 22, 172. (2011).
13. D. Persaud-Sharma, and A. McGoron, *J. Biomim. Biomater. Tissue Eng.* 12, 25. (2012).
14. R. Hou, J. Victoria-Hernandez, P. Jiang, R. Willumeit-Römer, B. Luthringer-Feyerabend, S. Yi, D. Letzig, and F. Feyerabend, *Acta Biomater.* 97, 608. (2019).
15. F. Witte, N. Hort, C. Vogt, S. Cohen, K.U. Kainer, R. Willumeit, and F. Feyerabend, *Curr. Opin. Solid State Mater. Sci.* 12, 63. (2008).
16. E. Mostaed, M. Sikora-Jasinska, L. Wang, A. Mostaed, I.M. Reaney, and J.W. Drelich, *JOM* 72, 1880. (2020).
17. B.P. Zhang, Y. Wang, and L. Geng, *Biomaterials-Physics and Chemistry*, Ed. R. Pignatello, (Rijeka: Intech, 2011), pp. 183-204.
18. D. Annur, F.P. Lestari, A. Erryani, M.I. Amal, L.S. Sitorus, and I. Kartika, *AIP Conf. Proc.* 1725, 020032. (2016).
19. W. Du, K. Liu, K. Ma, Z. Wang, S. Li, and J. Magnes, *Alloys* 6, 1. (2018).
20. J. Lee, H. Han, K. Han, J. Park, H. Jeon, M. Ok, H. Seok, J. Ahn, K. Lee, D. Lee, S. Yang, S. Cho, P. Cha, H. Kwon, T. Nam, J.H.L. Han, H. Rho, K. Lee, Y. Kim, and D. Mantovani, *Proc. Natl. Acad. Sci. USA* 113, 716. (2016).
21. T. Kokubo, and H. Takadama, *Biomaterials* 27, 2907. (2006).
22. Y. Lu, A. Bradshaw, Y.L. Chiu, and I. Jones, *Mater. Sci. Forum* 765, 788. (2013).
23. B. Denkena, and A. Lucas, *CIRP Ann.* 56, 113. (2007).
24. P. Chakraborty Banerjee, S. Al-Saadi, L. Choudhary, S.E. Harandi, and R. Singh, *Materials* 12, 136. (2019).
25. G.L. Hao, F.S. Han, and W.D. Li, *J. Porous Mater.* 16, 251. (2009).
26. C.S.S. de Oliveira, S. Griza, M.V. de Oliveira, A.A. Ribeiro, and M.B. Leite, *Powder Technol.* 281, 91. (2015).
27. N. Li, and Y. Zheng, *J. Mater. Sci. Technol.* 29, 489. (2013).
28. M. Peron, P.C. Skaret, A. Fabrizi, A. Varone, R. Montanari, H.J. Roven, P. Ferro, P. Berto, and J. Torgersen, *J. Mech. Behav. Biomed. Mater.* 106, 103724. (2020).
29. Y. Min, L. Debaio, Z. Runfang, and C. Minfang, *Rare Met Mater. Eng.* 47, 93. (2018).
30. Z. Li, X. Gu, S. Lou, and Y. Zheng, *Biomaterials* 29, 1329. (2008).
31. M.C. Delgado, F.R. García-Galvan, I. Llorente, P. Pérez, P. Adeva, and S. Feliu, *Corros. Sci.* 123, 182. (2017).
32. G.L. Song, *Corrosion of magnesium alloys* (Woodhead, Oxford, 2011).
33. F. Witte, V. Kaese, H. Haferkamp, E. Switzer, A. Meyer-Lindenberg, C.J. Wirth, and H. Windhagen, *Biomaterials* 26, 3557. (2005).
34. Y. Chen, S. Zhang, J. Li, Y. Song, C. Zhao, and X. Zhang, *Mater. Lett.* 64, 1996. (2010).
35. J.M. Rúa, A.A. Zuleta, J. Ramírez, and P. Fernández-Morales, *Surf. Coat. Technol.* 360, 213. (2019).

Publisher's Note Springer Nature remains neutral with regard to jurisdictional claims in published maps and institutional affiliations.